Solar Phys (2016) 291:3303–3315
DOI 10.1007/s11207-016-1018-7

WAVES IN THE SOLAR CORONA

Simultaneous Longitudinal and Transverse Oscillations in an Active-Region Filament

Vaibhav Pant[1] · **Rakesh Mazumder**[1,2] · **Ding Yuan**[3] ·
Dipankar Banerjee[1,2] · **Abhishek K. Srivastava**[4] ·
Yuandeng Shen[5]

Received: 15 February 2016 / Accepted: 12 November 2016 / Published online: 21 November 2016

Abstract We report on the co-existence of longitudinal and transverse oscillations in an active-region filament. On March 15, 2013, an M1.1 class flare was observed in Active Region AR 11692. A coronal mass ejection (CME) was found to be associated with the flare. The CME generated a shock wave that triggered the oscillations in a nearby filament, situated south-west of the active region as observed from National Solar Observatory (NSO) *Global Oscillation Network Group* (GONG) Hα images. In this work we report the longitudinal oscillations in the two ends of the filament, which co-existed with the transverse oscillations. We propose a scenario in which an incoming shock wave hits the filament obliquely and triggers both longitudinal and transverse oscillations. Using the observed parameters, we estimate the lower limit of the magnetic field strength. We use a simple pendulum model with gravity as the restoring force to estimate the radius of curvature. We also calculate the mass accretion rate that causes the filament motions to damp quite fast.

Keywords Sun, oscillation · Sun, filament · Sun, magnetic field

---

Waves in the Solar Corona: From Microphysics to Macrophysics
Guest Editors: Valery M. Nakariakov, David J. Pascoe, and Robert A. Sych

Electronic supplementary material The online version of this article (doi:10.1007/s11207-016-1018-7) contains supplementary material, which is available to authorised users.

✉ V. Pant
vaibhav@iiap.res.in

[1] Indian Institute of Astrophysics, Koramangala, Bangalore 560034, India

[2] Center of Excellence in Space Sciences, IISER Kolkata, Mohanpur 741246, West Bengal, India

[3] Jeremiah Horrocks Institute, University of Central Lancashire, Preston, UK

[4] Indian Institute of Technology (BHU), Varanasi, India

[5] Yunnan Observatories, Chinese Academy of Sciences, Kunming 650216, China

1. Introduction

Filaments support both longitudinal and transverse oscillations (see, Arregui, Oliver, and Ballester, 2012). The oscillations in the filaments can be used to diagnose the local plasma conditions and magnetic field by applying the principle of magnetohydrodynamic (MHD) seismology (see, Nakariakov and Verwichte, 2005; Andries, Arregui, and Goossens, 2005). These oscillations are broadly classified as large amplitude (Tripathi, Isobe, and Jain, 2009) and small amplitude (Oliver and Ballester, 2002) oscillations. Large amplitude transverse oscillations, where a filament oscillates as whole, are often associated with the disturbances coming from nearby flares (Ramsey and Smith, 1966; Isobe and Tripathi, 2006; Okamoto *et al.*, 2004; Hershaw *et al.*, 2011; Schmieder *et al.*, 2013; Pant *et al.*, 2015). In contrast, large amplitude longitudinal oscillations are always found to be associated with small energetic events such as a subflare at one leg of the filament (Jing *et al.*, 2003), a small flare in a nearby active region (Jing *et al.*, 2006; Vršnak *et al.*, 2007; Li and Zhang, 2012) or jets (Luna *et al.*, 2014). There have been several reports on large amplitude longitudinal oscillations (Jing *et al.*, 2003, 2006; Vršnak *et al.*, 2007; Luna and Karpen, 2012; Luna, Díaz, and Karpen, 2012; Zhang *et al.*, 2012; Luna *et al.*, 2014). Luna and Karpen (2012) developed a one-dimensional (1D) self-consistent model that explained both restoring force and damping of large amplitude longitudinal oscillations. The model is analogous to an oscillating pendulum assuming the radius of curvature of the magnetic dip as the length of the pendulum. Luna *et al.* (2014) used this model to explain the strong damping of large amplitude longitudinal oscillations observed in filament threads. Recently, Luna *et al.* (2016) performed 2D non-linear time-dependent MHD simulations where a magnetic field can become distorted in response to the mass loading. The authors have reported that a simple pendulum model can be used to characterise the large amplitude longitudinal oscillations even in a scenario where the magnetic field responds to the plasma motions.

Damping of oscillations have been observed in large amplitude transverse oscillations (Hershaw *et al.*, 2011; Pant *et al.*, 2015). Goossens, Andries, and Arregui (2006), Arregui *et al.* (2007) used seismology to combine the damping time and period of oscillations in a consistent manner to estimate the magnetic field strength and inhomogeneity length scale in the coronal loops. Arregui *et al.* (2008) applied the same technique to the oscillating threads of a prominence. Pant *et al.* (2015) applied this technique to estimate the magnetic field and the inhomogeneity length scale of a filament as whole.

In addition to transverse oscillations, large amplitude longitudinal oscillations are also found to be damped (Luna and Karpen, 2012; Luna *et al.*, 2014). Unlike transverse oscillations, which are now believed to be damped by resonant absorption, the damping mechanisms in longitudinal oscillations are not well understood. Several damping mechanisms have been proposed, *e.g.* energy leakage (Kleczek and Kuperus, 1969), dissipation (Tripathi, Isobe, and Jain, 2009), but these mechanisms are under debate. However, mass accretion due to the condensation of filament material (Luna and Karpen, 2012; Luna *et al.*, 2014, 2016; Ruderman and Luna, 2016) is shown to be a promising way to explain the damping of longitudinal oscillations in a filament. Recently, Ruderman and Luna (2016) have reported the evidence of strong damping of longitudinal oscillations in the filament threads that are modelled as a curved magnetic tube.

Shen *et al.* (2014) reported that an incoming shock wave can trigger longitudinal and transverse oscillations in filaments depending on the interaction angle between the filament and the shock wave. Gilbert *et al.* (2008) has reported the co-existence of two transverse oscillation modes in a filament, one in the plane of sky and another along the line of sight. These modes occurred in response to a Moreton wave. Both modes were perpendicular

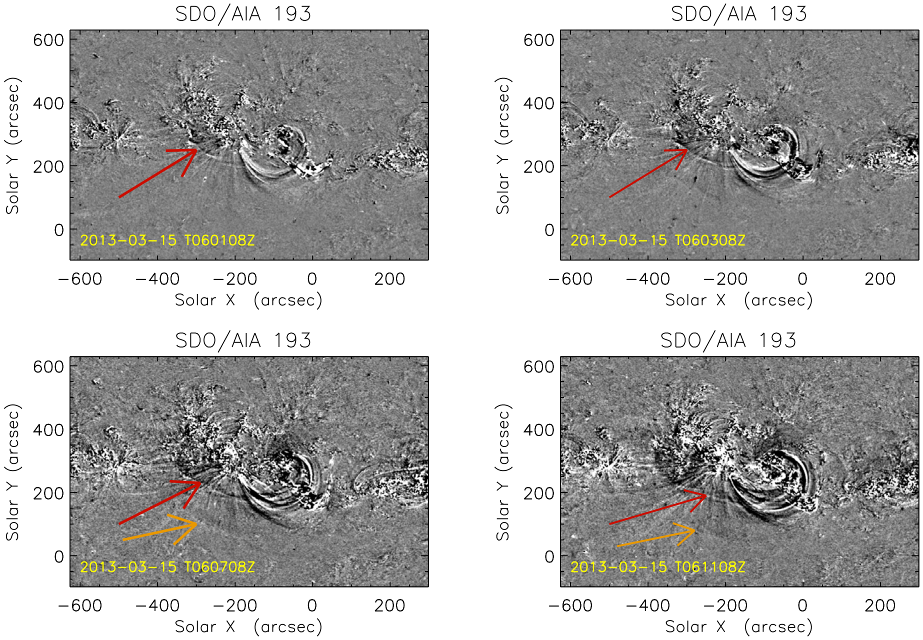

Figure 1 Difference images of AIA 193 Å at four different time instances. Arrows in red and orange represent the shock front.

to the filament axis. In this work, we report a unique observation of the co-existence of large amplitude damped longitudinal oscillations and large amplitude damped transverse oscillations in an active-region filament. The article is organised as follows. In Section 2 we describe the observations. In Section 3 we discuss the methods of the data analysis. We present the results in Section 4, which is followed by the discussion and conclusions in Section 5.

2. Observation

An M1.1 class flare was observed by the GOES satellite in Active Region AR 11692 on March 15, 2013. The flare was associated with a halo coronal mass ejection (CME). The flare created a global disturbance in the active region. The CME associated with the flare produced a shock wave. To observe shock fronts, we created running-difference images of AIA 193 Å. The shock fronts are marked with red and orange arrows in Figure 1. It is evident from Figure 1 that the shock fronts are moving outward.

A filament was lying to the south-west of the active region as seen in Hα images from NSO/GONG (Figure 2). NSO/GONG provides full-disk observation of the Sun in 6563 Å (Hα). It has a pixel resolution of $\sim 1.07''$ and a cadence of 1 sec. The observational data used in this study are obtained from 06:00:54 UT to 10:22:54 UT. The flare started at 05:46:00 UT, peaked at 06:58:00 UT, and ended at 08:35:00 UT as recorded in the GOES catalogue. We note that immediately after the onset of the flare, oscillations were triggered in the filament.

Filaments consist of fine threads that are not often seen in GONG Hα images because of its poor spatial resolution. Therefore, we used the images from the extreme ultraviolet

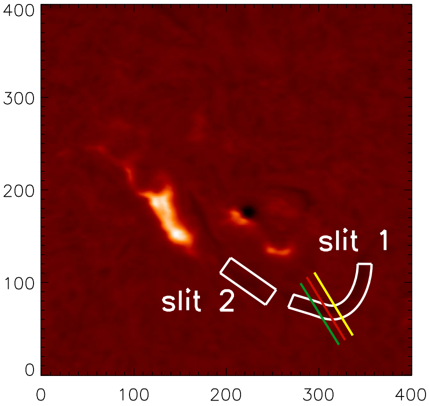

Figure 2 NSO/GONG Hα image of the filament lying south-west of Active Region AR 11692. The image was taken on March 15, 2013 at 06:55:22 UT. The bright ribbons correspond to the M1.1 class flare. Two broad artificial slices along the axis of the filament, used to generate x – t maps, are overplotted. Three artificial slits perpendicular to the axis of the filament are overplotted in green, red, and yellow, which were used in Pant *et al.* (2015) to investigate the transverse oscillations.

(EUV) passbands of the *Atmospheric Imaging Assembly* (AIA) onboard the *Solar Dynamics Observatory* (SDO). The AIA instrument provides almost simultaneous full-disk images of the Sun in seven EUV bands. It has a spatial resolution of 1.3″, a pixel size of 0.6″, and a cadence of 12 s (Lemen *et al.*, 2012). We find that the filament consists of several threads that are seen more clearly in AIA 171 Å than in any other EUV passband of AIA. Therefore, we use AIA 171 Å for the further analysis. Moreover, we find that shortly after the oscillations started, the full-disk images of the Sun were not available from 06:22:23 UT to 07:36:00 UT. Thus, the first cycle of oscillations is not seen in AIA 171 Å.

We overplot the contours of the filament as seen in GONG Hα over the magnetogram obtained from the *Helioseismic and Magnetic Imager* (HMI) onboard SDO (Figure 3). We find that the filament lies above the region that separates positive and negative polarities. We note from the movie (available online) that at 06:11:59 UT, *i.e.* before eruption, the filament material as enclosed in two different contours is part of the same filament (Pant *et al.*, 2015, right panel of Figure 1).

By careful inspection of the Hα images in the movie (available online), it appears that both longitudinal and transverse oscillations are present simultaneously in the filament. In the movie we mark the filament in AIA images with a green arrow. The transverse oscillations in the filament under study have been reported in Pant *et al.* (2015). In this article we focus on longitudinal oscillations at two parts of the filament adjacent to its two ends.

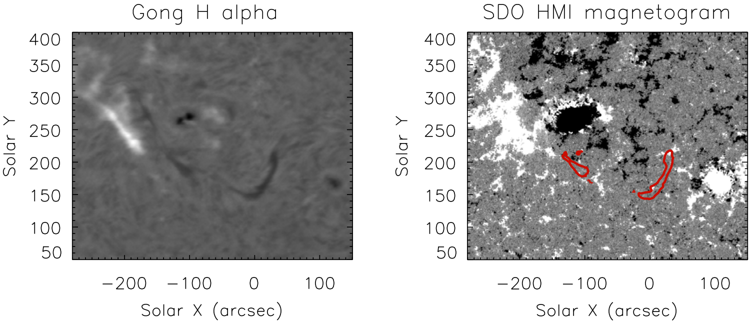

Figure 3 Left: GONG Hα image taken on March 15, 2013 at 09:28:45 UT. Right: HMI magnetogram taken at 09:28:59 UT. Overplotted red contours outline the position of the filament.

3. Data Analysis

3.1. GONG Hα

To investigate the longitudinal oscillations in GONG Hα images, we place two artificial broad slices, slit 1 and slit 2 along the axis of the filament as shown in Figure 2. The length (width) of the first and second slice is 130 pixel (15 pixel) and 60 pixel (20 pixel), respectively. The filament is oscillating in both transverse and longitudinal directions simultaneously. We choose broad slices so that the filament material remains inside the slices in spite of the transverse oscillations.

To further characterise the longitudinal oscillations in the filament, first we create a time-distance (x – t) map with time in x-axis and distance along the slice in y-axis for slits 1 and 2. The intensity along each column of the x – t map is fitted with a Gaussian curve. The mean value and one-sigma error of the intensity is estimated. Finally, the x – t map is fitted with a damped sinusoidal function to investigate the oscillation characteristics. Since the filament is oscillating and the amplitude of the oscillations is decreasing with time, it can be fitted with a damped sinusoidal function (assuming the mass of the filament to be constant) and represented as (Aschwanden *et al.*, 1999),

$$y(t) = c + A_{\mathrm{sin}} \sin(\omega t + \phi_{\mathrm{sin}}) e^{-t/\tau_{\mathrm{sin}}}, \tag{1}$$

where c is a constant, A_{sin} is the amplitude, τ_{sin} is the damping time, ω is the angular frequency, and ϕ_{sin} is the initial phase of sinusoidal function. The least-squares fitting is done using the function *MPFIT.pro* in Interactive Data Language (IDL) (Markwardt, 2009). It has been shown that if a filament accretes mass, then the Bessel function describes the oscillations better than the damped sinusoid (Luna and Karpen, 2012). Therefore, we fit the x – t map using a damped zeroth-order Bessel function of the first kind, represented by

$$y(t) = c_1 + A_{\mathrm{bes}} J_0(\omega t + \phi_{\mathrm{bes}}) e^{-t/\tau_{\mathrm{bes}}}, \tag{2}$$

where c_1 is a constant, A_{bes} is amplitude, ω is the angular frequency, τ_{bes} is the damping time, and ϕ_{bes} is the phase of the Bessel function.

3.2. AIA 171 Å

We repeat the analysis on AIA 171 Å images, but with only one artificial slice. The filament material at the position of slit 2 is not clearly seen in AIA 304, 171, and 193 Å because of overlying post-flare loops (see movie).

4. Results

4.1. GONG Hα

The period, damping time, and amplitude estimated from the fitting of a damped sinusoidal function represented by Equation (1) are summarised in Table 1. The period, damping time, and amplitude estimated from the fitting of a damped zeroth-order Bessel function of the first kind represented by Equation (2) is summarised in Table 2. In the right panel of Figure 4, we overplot dashed green lines at three time instances. It is evident that both ends of the filament started oscillating in different phase. It is also worth noting that the oscillations started at different times in the two ends of the filament.

Table 1 Table of parameters of the damped sine fitting

Slit No.	Displacement amplitude (in Mm)	Period (in min)	Damping time (in min)	Velocity amplitude (in $\mathrm{km\,s^{-1}}$)
slice 1	37 ± 15	57 ± 2	46 ± 8	69 ± 30
slice 2	6 ± 1	58 ± 1	119.3 ± 0.1	15 ± 2

Table 2 Table of parameters of the modified Bessel function fitting

Slit No.	Displacement amplitude (in Mm)	Period (in min)	Damping time (in min)	Velocity amplitude (in $\mathrm{km\,s^{-1}}$)
slice 1	27 ± 12	57 ± 2	51 ± 10	49 ± 25
slice 2	6 ± 2	58 ± 1	204 ± 38	11 ± 4

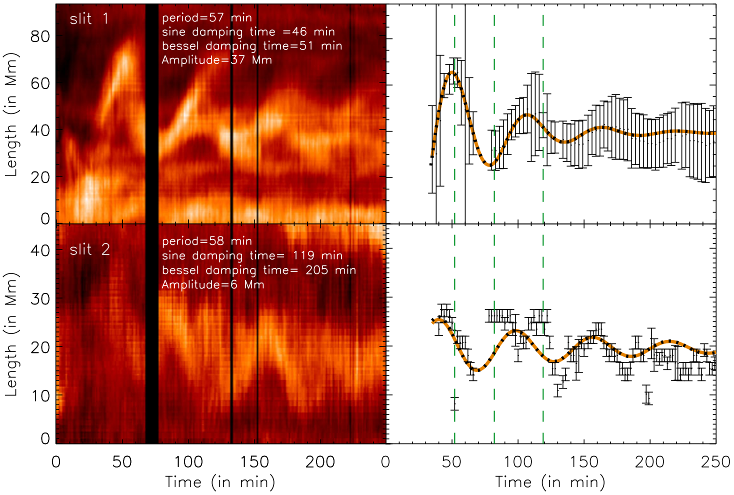

Figure 4 The upper left panel shows the x – t map of slit 1. The starting time is March 15, 2013 at 06:00:54 UT. The thick black vertical strip represents a data gap between 07:07:54 UT to 07:18:54 UT. The time period, amplitude, and damping time obtained from fitting is mentioned at the top of the plot. The lower left panel is the same as the upper left panel, but for slit 2. In the upper right panel we plot the fitted damped sinusoidal curve with a one-sigma error bar. The lower right panel is the same for slit 2. Three vertical dashed lines over plotted at three time instances show that the oscillations started with different phases. The dotted black curve represents the best-fit damped sinusoidal function, while the orange curve represents the damped Bessel function.

4.2. AIA 171 Å

The oscillation period is found to be 57±3 min, which is similar to the period estimated at the position of slit 1 in GONG Hα. The damping time is estimated to be 100 min, which is longer than the damping time estimated using slit 1 in GONG Hα images. The oscillation amplitude is found to be 10 Mm, which is less than the amplitude measured in GONG Hα images. The main reason for the long damping time and smaller amplitude is that the first oscillation cycle is missed in AIA 171 Å images, therefore the oscillations start after 100 min, as shown in Figure 5 (right panel). We note from Figure 4 (top right panel) that the

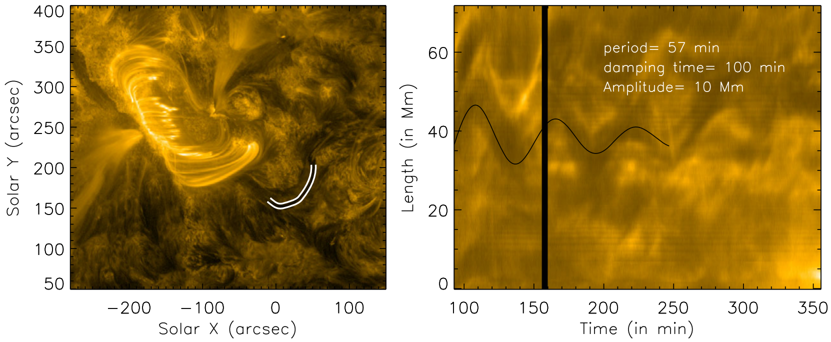

Figure 5 The left panel shows the AIA 171 Å image taken at March 15, 2013 at 08:51:23 UT with artificial slice overplotted on the filament. The right panel represents the x – t map corresponding to the curve artificial slice shown in the left panel. The starting time is March 15, 2013 at 06:00:54 UT. The thick black vertical strip represents the data gap between 07:07:54 UT to 07:18:54 UT. The black curve represents the best-fit sinusoidal function. The time period, amplitude, and damping time obtained from fitting is listed at the top.

estimated damping time of oscillations and amplitude are strongly dependent on the first oscillation cycle. If the first oscillation cycle is missed, then the damping time is longer and the amplitude is smaller. Another reason can be that the filament threads apparently merge and separate during the oscillations. This may be attributed to the fact that multiple threads are stacked along the line of sight. If they are not moving in phase, then it may appear that they are merging and separating. This is probably also related to the presence of transverse oscillations because this effect is not reported in earlier studies (Luna and Karpen, 2012) where only longitudinal oscillations were present. Therefore, choosing the thread that is associated with the oscillations is very challenging (see right panel of Figure 5). It is worth noting at this point that we did not fit a damped Bessel function to the AIA dataset because, as said above, the first oscillation cycle is missed, thus the Bessel function will not give the correct estimate of the damping time.

4.3. Radius of Curvature of the Magnetic Dip

Filament material is supported by the magnetic fields against gravity. We use a simple pendulum model to estimate the oscillation parameters (Luna and Karpen, 2012). Assuming the restoring force to be gravity, we obtain the following equation

$$\omega = \frac{2\pi}{P} = \sqrt{\frac{g_0}{R}}, \tag{3}$$

where g_0 is the Sun's surface gravity, ω is the oscillation frequency, P is the period of oscillation, and R is the radius of curvature. Using Equation (3), the radius of curvature in GONG Hα images is estimated to be $\sim$ 80 Mm and 85 Mm at the position of dip 1 (where the first slice is placed) and dip 2 (where the second slice is placed; see Figure 2), respectively. Similarly, the radius of curvature at the location of dip 1 (see left-hand panel of Figure 5, where the artificial slice is placed) in AIA 171 Å is estimated to be 80 Mm.

4.4. Estimation of Magnetic Field Strength

We calculate a lower limit of the magnetic field strength, assuming that magnetic stress is balanced by the weight of the filament material present in a dip (Luna and Karpen, 2012), using the following expression,

$$B(G) \geq 26\left(\frac{n_e}{10^{11}}\right)^{\frac{1}{2}} P, \tag{4}$$

where B is the magnetic field, n_e is the electron number density in cm^{-3}, and P is the oscillation period in hours. Here we use the typical value of the electron number density 10^{11} cm^{-3} as reported in Labrosse *et al.* (2010). Therefore, the minimum magnetic field strength is estimated to be $\sim (25 \pm 1)$ G in dips 1 and 2, which is consistent with the typical values of the measured magnetic fields in the filaments (Labrosse *et al.*, 2010; Mackay *et al.*, 2010). Since the period of oscillation is estimated to be the same using AIA 171 Å, the estimated magnetic field strength remains unchanged.

4.5. Estimation of the Mass Accretion Parameter

In the model given by Luna and Karpen (2012), the damping of longitudinal oscillations in threads of the filaments is explained by the accretion of filament material. We calculate the mass accretion rate from the best-fit parameters of the damped Bessel function (represented by Equation (2)), using the following relation (Luna *et al.*, 2014),

$$\alpha = \frac{\omega m_0}{\phi_{\mathrm{bes}}},$$

where m_0 is the initial mass of the filament, and ω and ϕ_{bes} are obtained from fitting the damped Bessel function. The mass of a filament, m_0, can be calculated as $m_0 = 1.27 m_p n_e \pi r^2 L$, where r and L are the radius and the length of the thread of the filament. We take the typical radius of a filament thread to be 100 km as assumed in Luna *et al.* (2014). The length of the thread is estimated using an $\mathrm{x-t}$ map, as shown in Figure 4 (top panel). As explained above, the artificial slit is placed along the length of the filament. Thus the extent of the brightness along each column of the $\mathrm{x-t}$ map gives an estimate of the length of the filament thread at a particular time instance. The length of the filament thread is measured at various time instances (*i.e.* along different columns) from the start to the end of the oscillations. Finally, we estimate the mean value of the length of the filament thread $\sim 23 \pm 7$ Mm at the position of slit 1. Following the above procedure, the length of the filament thread at the position of slit 2 is estimated to be $\sim 10 \pm 4$ Mm. It should be borne in mind that estimating the length of the filament thread at the position of slit 2 is uncertain because the oscillations are not clearly seen in the $\mathrm{x-t}$ maps, as shown in the bottom panel of Figure 4. Under these assumptions, we estimated the mass accretion rate at the position of slits 1 and 2 to be $\sim (51 \pm 17 \times 10^6\ \mathrm{kg\,hr^{-1}})$ and $(192 \pm 72 \times 10^6\ \mathrm{kg\,hr^{-1}})$, respectively. The derived mass accretion rate at the position of slit 1 is comparable to those reported in earlier studies (Luna *et al.*, 2014). It should be noted that at the position of slit 2 the mass accretion rate is higher, while the damping time is longer. One of the reasons for this discrepancy is the uncertainty in the fitting parameters. The mass accretion rate depends on the phase of the Bessel function, which is estimated from the best-fit parameters. Therefore, if the fitting of a function is poor, then the value of phase will have large errors and thus cannot be trusted.

4.6. Possible Existence of Both Longitudinal and Transverse Waves Driven by Kink Oscillations

In this subsection we investigate the possibility that both longitudinal and transverse oscillations may be driven by kink oscillations. We assume the filament has the shape of a cylinder embedded in a uniform plasma with low plasma β. The magnetic field is assumed to be constant inside the cylinder, and the effects of gravity are ignored. The model set-up is similar to the one described in Yuan and Van Doorsselaere (2016). To derive the variation of thermodynamic quantities, linearised ideal MHD equations are used (see Ruderman and Erdélyi, 2009),

$$\rho = -\nabla \cdot (\rho_0 \xi), \tag{5}$$

$$\rho_0 \frac{\partial^2 \xi}{\partial t^2} = -\nabla(p + \mathbf{b} \cdot \mathbf{B}_0/\mu_0) + \frac{1}{\mu}\big[(\mathbf{B}_0 \cdot \nabla)\mathbf{b} + (\mathbf{b} \cdot \nabla)\mathbf{B}_0\big], \tag{6}$$

$$\mathbf{b} = \nabla \times (\boldsymbol{\xi} \times \mathbf{B}_0), \tag{7}$$

$$p - C_s^2 \rho = \xi \cdot \big(C_s^2 \nabla \rho_0 - \nabla p_0\big), \tag{8}$$

where ξ is the Lagrange displacement vector, ρ, p, and $\mathbf{b}$ are perturbed quantities, while ρ_0, p_0, and $\mathbf{B}_0$ are unperturbed quantities. Neumann boundary conditions are assumed at $r = a$

$$[P_T]_{r=a} = 0,$$

$$[\xi_r]_{r=a} = 0,$$

and Dirichlet boundary conditions are assumed at $r = 0, \infty$

$$P_T|_{r=0} < \infty,$$

$$\xi^2|_{r=0} = \infty,$$

$$P_T|_{r\to\infty} = 0,$$

$$\xi|_{r\to\infty} = 0,$$

where P_T is the total pressure.

For a filament, we define ω, ω_A, ω_T as kink, Alfvén, and tube oscillation frequency, respectively, and the tube speed, C_T, is given by $C_T = \frac{C_A C_s}{\sqrt{C_A^2 + C_s^2}}$, where $C_A = \frac{B_0}{\sqrt{\mu_0 \rho_0}}$ is the Alfvén speed and $C_s = \sqrt{\frac{\gamma p_0}{\rho_0}}$ is the sound speed. B_0, p_0, and ρ_0 are the equilibrium magnetic field, plasma pressure, and plasma density, respectively, and μ_0 is the magnetic permeability in free space. For a kink mode ($m = 1$), the total pressure perturbation, $P_{T1} = p + \mathbf{b} \cdot \mathbf{B}_0/\mu_0$, in the filament is assumed to be

$$P_{T1} = A R(r) \cos(\omega t) \sin(kz) \cos(\phi), \tag{9}$$

where A is the amplitude of the total perturbed pressure. Since a kink mode is not axisymmetric, $\cos(\phi)$ dependence is assumed. Substituting Equation (9) into Equations (5)–(8) yields

$$\frac{\mathrm{d}^2 P_{T1}}{\mathrm{d}r^2} + \frac{\mathrm{d}P_{T1}}{r\,\mathrm{d}r} - \left(\kappa_r^2 + \frac{1}{r^2}\right) P_{T1} = 0, \tag{10}$$

where

$$\kappa_r^2 = \frac{(\omega_s^2 - \omega^2)(\omega_A^2 - \omega^2)}{(\omega_s^2 + \omega_A^2)(\omega_T^2 - \omega^2)} k^2, \tag{11}$$

where $\omega_s^2 = k^2 C_s^2$. Equation (10) should also hold true for $R(r)$. In this work we confine ourselves to the inside of the flux tube. From solving Equation (10) for $R(r)$, we therefore obtain

$$R = J_1\big(|\kappa_r|r\big).$$

In cylindrical coordinates, v_r is the perturbed velocity amplitude of the transverse oscillation and v_z is the perturbed velocity amplitude of the longitudinal oscillation. Inside the cylinder, the perturbed radial and axial components of the velocity amplitude are defined as (see Yuan and Van Doorsselaere, 2016, for details)

$$v_r = -\frac{r\,\mathrm{d}R}{R\,\mathrm{d}r}\sin(\omega t)\sin(kz)\cos(\phi)$$

and

$$v_z = -\frac{C_T^2}{C_A^2}kr\frac{\omega^2 - \omega_A^2}{\omega^2 - \omega_T^2}\sin(\omega t)\cos(kz)\cos(\phi).$$

Thus, the axial-to-radial velocity amplitude ratio is given by the following expression:

$$\frac{v_z}{v_r} = k\frac{C_T^2}{C_A^2}\frac{R}{\frac{\mathrm{d}R}{\mathrm{d}r}}\frac{\omega^2 - \omega_A^2}{\omega^2 - \omega_T^2}\cot(kz). \tag{12}$$

We take the length of slit 2 as the length of the filament, which is estimated to be 90 Mm. The radius of the filament is estimated to be ~ 1 Mm. It is important to note that here we assume the length of the flux tube (modelled as a filament) as the length of the slit covering the filament material because here we compare longitudinal oscillations with the transverse oscillations as reported by Pant *et al.* (2015), where the authors assumed that the filament was oscillating as a whole in the transverse direction. To estimate the ratio of the axial-to-radial velocity amplitude, we choose three slit positions that we show in green, red, and yellow lines in Figure 2; these were used by Pant *et al.* (2015). From observations, we find that the ratio of the longitudinal velocity amplitude to the transverse velocity amplitude at these locations is 3.92, 3.26, and 2.22, respectively. Using Equation (12), we estimate the ratio to be 4×10^{-4}, 2×10^{-4}, and 1×10^{-5}, respectively, assuming the typical value of the sound speed in the chromosphere to be 15 $\mathrm{km\,s^{-1}}$, the Alfvén speed at the three slit positions as 82, 88, and 91 $\mathrm{km\,s^{-1}}$, respectively, and the perturbation frequency (assumed to be equal to the kink oscillation frequency) to be 117, 124, and 128 $\mathrm{km\,s^{-1}}$, respectively (see, Pant *et al.*, 2015). It should be borne in mind that a linear analysis is presented here. Considering the observed displacement to be large, non-linear effects would become important. Therefore to model such events, more studies are needed. Nevertheless, from the above analysis, we note that it is almost impossible to detect longitudinal oscillation in low-β plasma as a result of a fast kink mode in our observation. Therefore, large amplitude longitudinal oscillations cannot be the kink mode.

5. Interaction of the Shock with the Filament

In this section, we explore the most likely mechanism for driving the longitudinal and transverse oscillations in a filament channel. Shen *et al.* (2014) reported that shock waves can interact with filaments in two possible geometries. If shock waves occur such that the normal vector to the shock wave is perpendicular to the filament axis, then a filament oscillates

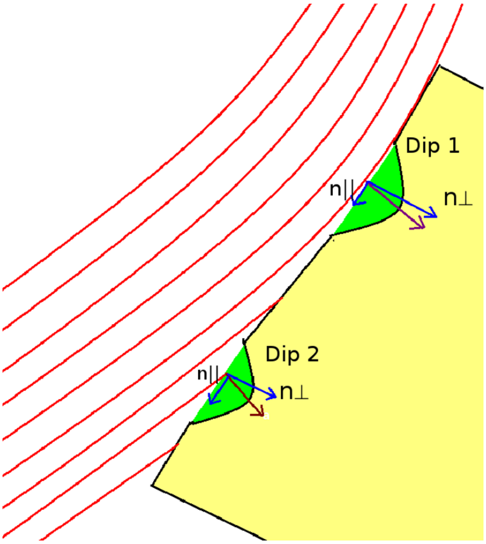

Figure 6 A cartoon depicting the interaction of a shock wave with a filament. The filament has two magnetic dips, dip 1 and dip 2. The filament material is shown in green. The shock wave front is represented by red curves. The normal vector to the shock wave front is shown in dark red. Arrows in blue represent the parallel and perpendicular components of the normal vector.

in the transverse direction, while if the shock wave interacts with a filament such that the normal vector of the shock wave is parallel to the filament axis, then a filament oscillates in the longitudinal direction. Here we propose a more general scenario, where a shock wave interacts obliquely with the filament such that the filament material oscillates in both transverse and longitudinal directions, as revealed from our observations. The position of the shock fronts in our observations are clearly seen in Figure 1. However, it should be borne in mind that from observations it is not straightforward to determine the direction of the shock with respect to the filament because the filament is in close proximity to the active region and is associated with overlying loops that expand in response to the shock wave. This makes it extremely difficult to determine the orientation of the shock wave.

We depict this by a cartoon in Figure 6. We show that when a shock wave hits a filament obliquely, the normal vector to the wave front, $\hat{n}$ (shown in dark red), can be decomposed into perpendicular ($n_{\perp}$) and parallel ($n_{||}$) components as shown in Figure 6 in blue. The component parallel to the filament axis triggers the longitudinal oscillations in the filament, while the component perpendicular to the filament axis triggers the transverse oscillations in the filament. Thus the shock front interacts with the filament at dip 1 and displaces the filament material in both transverse and longitudinal directions. Similarly, in dip 2 the shock front displaces the plasma in both transverse and longitudinal directions, but at a different time. With this schematic picture we can explain the different start times of the longitudinal oscillation at the two ends of the filament. However, with this scenario, we would expect the transverse oscillations to be present at the locations of both dips, but transverse oscillations are only observed at the location of dip 1. It is worth noting that this is the simple geometry. In principle, many parts of the shock wave can interact with the filament at different orientations and can excite different modes. More detailed studies are needed to confirm this.

6. Summary and Conclusions

In this work, we find the co-existence of longitudinal and transverse oscillations in an active-region filament as observed by NSO/GONG Hα. The oscillations are triggered by the interaction of a shock wave with the filament. We find that the oscillations in the two ends of the filament started with different phases, but with an almost identical oscillation period. We note that the longitudinal oscillations at the two slit positions started at different times (see Figure 4), possibly because the shock wave front interacted with the two parts of the filament at different time instances. We depict this with a schematic diagram (see Figure 6).

The damping time at the position of slit 1 is estimated to be 46 minutes. This is slightly too long compared to the earlier reports (Tripathi, Isobe, and Jain, 2009) and comparable to what is reported in Luna *et al.* (2014). Luna and Karpen (2012) suggested that the mass accretion of the filament material is responsible for damping. We find the mass accretion rate to be $51 \pm 17 \times 10^6\ \mathrm{kg\,hr^{-1}}$ at the position of slit 1 and $192 \pm 72 \times 10^6\ \mathrm{kg\,hr^{-1}}$ at the position of slit 2, which is comparable with the earlier reports (Luna *et al.*, 2014). We performed the filament seismology and estimated the magnetic field strength at two dip locations. We estimated the lower limit of the magnetic field strength $\sim (25 \pm 1)$ G at the location of both the slices, which is consistent with typical values of the measured magnetic field from observation (Mackay *et al.*, 2010). We also calculate the radius of curvature of the two magnetic dips of the filament as 80 Mm and 85 Mm for dips 1 and 2, respectively.

Based on our observations, we exclude the possibility that transverse and longitudinal oscillations could be simultaneously driven by a fast kink mode. Longitudinal oscillations due to a kink wave may be present, but their amplitude is much smaller than the amplitude of the longitudinal oscillations observed in this case. This shows that transverse and longitudinal oscillations exist independently in the filament under study.

Acknowledgement We would like to thank the referee for the valuable comments that have improved the presentation of this article.

Disclosure of Potential Conflicts of Interest The authors declare that they have no conflicts of interest.

References

Andries, J., Arregui, I., Goossens, M.: 2005, Determination of the coronal density stratification from the observation of harmonic coronal loop oscillations. *Astrophys. J. Lett.* **624**, L57. DOI. ADS.

Arregui, I., Andries, J., Van Doorsselaere, T., Goossens, M., Poedts, S.: 2007, MHD seismology of coronal loops using the period and damping of quasi-mode kink oscillations. *Astron. Astrophys.* **463**, 333. DOI. ADS.

Arregui, I., Oliver, R., Ballester, J.L.: 2012, Prominence oscillations. *Living Rev. Solar Phys.* **9**, 2. DOI. ADS.

Arregui, I., Terradas, J., Oliver, R., Ballester, J.L.: 2008, Damping of fast magnetohydrodynamic oscillations in quiescent filament threads. *Astrophys. J. Lett.* **682**, L141. DOI. ADS.

Aschwanden, M.J., Fletcher, L., Schrijver, C.J., Alexander, D.: 1999, Coronal loop oscillations observed with the transition region and coronal explorer. *Astrophys. J.* **520**, 880. DOI. ADS.

Gilbert, H.R., Daou, A.G., Young, D., Tripathi, D., Alexander, D.: 2008, The filament-Moreton wave interaction of 2006 December 6. *Astrophys. J.* **685**, 629. DOI. ADS.

Goossens, M., Andries, J., Arregui, I.: 2006, Damping of magnetohydrodynamic waves by resonant absorption in the solar atmosphere. *Phil. Trans. Roy. Soc. London Ser. A, Math. Phys. Sci.* **364**, 433. DOI. ADS.

Hershaw, J., Foullon, C., Nakariakov, V.M., Verwichte, E.: 2011, Damped large amplitude transverse oscillations in an EUV solar prominence, triggered by large-scale transient coronal waves. *Astron. Astrophys.* **531**, A53. DOI. ADS.

Isobe, H., Tripathi, D.: 2006, Large amplitude oscillation of a polar crown filament in the pre-eruption phase. *Astron. Astrophys.* **449**, L17. DOI. ADS.

Jing, J., Lee, J., Spirock, T.J., Xu, Y., Wang, H., Choe, G.S.: 2003, Periodic motion along a solar filament initiated by a subflare. *Astrophys. J. Lett.* **584**, L103. DOI. ADS.

Jing, J., Lee, J., Spirock, T.J., Wang, H.: 2006, Periodic motion along solar filaments. *Solar Phys.* **236**, 97. DOI. ADS.

Kleczek, J., Kuperus, M.: 1969, Oscillatory phenomena in quiescent prominences. *Solar Phys.* **6**, 72. DOI. ADS.

Labrosse, N., Heinzel, P., Vial, J.-C., Kucera, T., Parenti, S., Gunár, S., Schmieder, B., Kilper, G.: 2010, Physics of solar prominences: I – Spectral diagnostics and non-LTE modelling. *Space Sci. Rev.* **151**, 243. DOI. ADS.

Lemen, J.R., Title, A.M., Akin, D.J., Boerner, P.F., Chou, C., Drake, J.F., Duncan, D.W., Edwards, C.G., Friedlaender, F.M., Heyman, G.F., Hurlburt, N.E., Katz, N.L., Kushner, G.D., Levay, M., Lindgren, R.W., Mathur, D.P., McFeaters, E.L., Mitchell, S., Rehse, R.A., Schrijver, C.J., Springer, L.A., Stern, R.A., Tarbell, T.D., Wuelser, J.-P., Wolfson, C.J., Yanari, C., Bookbinder, J.A., Cheimets, P.N., Caldwell, D., Deluca, E.E., Gates, R., Golub, L., Park, S., Podgorski, W.A., Bush, R.I., Scherrer, P.H., Gummin, M.A., Smith, P., Auker, G., Jerram, P., Pool, P., Soufli, R., Windt, D.L., Beardsley, S., Clapp, M., Lang, J., Waltham, N.: 2012, The Atmospheric Imaging Assembly (AIA) on the Solar Dynamics Observatory (SDO). *Solar Phys.* **275**, 17. DOI. ADS.

Li, T., Zhang, J.: 2012, SDO/AIA observations of large-amplitude longitudinal oscillations in a solar filament. *Astrophys. J. Lett.* **760**, L10. DOI. ADS.

Luna, M., Díaz, A.J., Karpen, J.: 2012, The effects of magnetic-field geometry on longitudinal oscillations of solar prominences. *Astrophys. J.* **757**, 98. DOI. ADS.

Luna, M., Karpen, J.: 2012, Large-amplitude longitudinal oscillations in a solar filament. *Astrophys. J. Lett.* **750**, L1. DOI. ADS.

Luna, M., Knizhnik, K., Muglach, K., Karpen, J., Gilbert, H., Kucera, T.A., Uritsky, V.: 2014, Observations and implications of large-amplitude longitudinal oscillations in a solar filament. *Astrophys. J.* **785**, 79. DOI. ADS.

Luna, M., Terradas, J., Khomenko, E., Collados, M., de Vicente, A.: 2016, On the robustness of the pendulum model for large-amplitude longitudinal oscillations in prominences. *Astrophys. J.* **817**, 157. DOI. ADS.

Mackay, D.H., Karpen, J.T., Ballester, J.L., Schmieder, B., Aulanier, G.: 2010, Physics of solar prominences: II – Magnetic structure and dynamics. *Space Sci. Rev.* **151**, 333. DOI. ADS.

Markwardt, C.B.: 2009, Non-linear least-squares fitting in IDL with MPFIT. In: Bohlender, D.A., Durand, D., Dowler, P. (eds.) *Astronomical Data Analysis Software and Systems XVIII*, *Astron. Soc. Pac. Conf. Ser.* **411**, 251. ADS.

Nakariakov, V.M., Verwichte, E.: 2005, Coronal waves and oscillations. *Living Rev. Solar Phys.* **2**, 3. DOI. ADS.

Okamoto, T.J., Nakai, H., Keiyama, A., Narukage, N., UeNo, S., Kitai, R., Kurokawa, H., Shibata, K.: 2004, Filament oscillations and Moreton waves associated with EIT waves. *Astrophys. J.* **608**, 1124. DOI. ADS.

Oliver, R., Ballester, J.L.: 2002, Oscillations in quiescent solar prominences observations and theory (invited review). *Solar Phys.* **206**, 45. DOI. ADS.

Pant, V., Srivastava, A.K., Banerjee, D., Goossens, M., Chen, P.-F., Joshi, N.C., Zhou, Y.-H.: 2015, MHD seismology of a loop-like filament tube by observed kink waves. *Res. Astron. Astrophys.* **15**, 1713. DOI. ADS.

Ramsey, H.E., Smith, S.F.: 1966, Flare-initiated filamei it oscillations. *Astron. J.* **71**, 197. DOI. ADS.

Ruderman, M.S., Erdélyi, R.: 2009, Transverse oscillations of coronal loops. *Space Sci. Rev.* **149**, 199. DOI. ADS.

Ruderman, M., Luna, M.: 2016, Damping of prominence longitudinal oscillations due to mass accretion. *Aston. Astrophys.* **591**, A131. DOI. ADS.

Schmieder, B., Kucera, T.A., Knizhnik, K., Luna, M., Lopez-Ariste, A., Toot, D.: 2013, Propagating waves transverse to the magnetic field in a solar prominence. *Astrophys. J.* **777**, 108. DOI. ADS.

Shen, Y., Liu, Y.D., Chen, P.F., Ichimoto, K.: 2014, Simultaneous transverse oscillations of a prominence and a filament and longitudinal oscillation of another filament induced by a single shock wave. *Astrophys. J.* **795**, 130. DOI. ADS.

Tripathi, D., Isobe, H., Jain, R.: 2009, Large amplitude oscillations in prominences. *Space Sci. Rev.* **149**, 283. DOI. ADS.

Vršnak, B., Veronig, A.M., Thalmann, J.K., Žic, T.: 2007, Large amplitude oscillatory motion along a solar filament. *Astron. Astrophys.* **471**, 295. DOI. ADS.

Yuan, D., Van Doorsselaere, T.: 2016, Forward modeling of standing kink modes in coronal loops. I. Synthetic views. *Astrophys. J. Suppl.* **223**, 23. DOI. ADS.

Zhang, Q.M., Chen, P.F., Xia, C., Keppens, R.: 2012, Observations and simulations of longitudinal oscillations of an active region prominence. *Astron. Astrophys.* **542**, A52. DOI. ADS.